Estimating the radiative forcing of carbonaceous aerosols over California based on satellite and ground observations

Yangyang Xu,[1] Ranjit Bahadur,[1] Chun Zhao,[2] and L. Ruby Leung[2]

Received 30 July 2013; revised 5 September 2013; accepted 12 September 2013; published 4 October 2013.

[1] Carbonaceous aerosols have the potential to impact climate directly through absorption of incoming solar radiation and indirectly by affecting cloud and precipitation. Recent modeling studies have made great efforts to simulate both the spatial and temporal distributions of carbonaceous aerosol's optical properties and radiative forcing. This study makes the first observationally constrained assessment of the direct radiative forcing of carbonaceous aerosols over California. By exploiting multiple observations (including ground sites and satellites), we constructed the distribution of aerosol optical depths and aerosol absorption optical depths (AAOD) over California for a 10 year period (2000–2010). We partitioned the total solar absorption into individual contributions from elemental carbon (EC), organic carbon (OC), and dust aerosols, using a newly developed scheme. Our results show that AAOD due to carbonaceous aerosols (EC and OC) at 440 nm was 50%–200% larger than natural dust, with EC contributing the bulk (70%–90%). Observationally constrained EC absorption agrees reasonably well with estimates from global and regional chemical transport models, but the models underestimate the OC AAOD by at least 50%. We estimated that the top of the atmosphere (TOA) forcing from carbonaceous aerosols was 0.7 W/m^2 and the TOA forcing due to OC was close to zero. The atmospheric heating of carbonaceous aerosol was 2.2–2.9 W/m^2, of which EC contributed about 80–90%. We estimated the atmospheric heating of OC at 0.1–0.4 W/m^2, larger than model simulations. EC reduction over the last two decades may have caused a surface brightening of 1.5–3.5 W/m^2.

Citation: Xu, Y., R. Bahadur, C. Zhao, and L. Ruby Leung (2013), Estimating the radiative forcing of carbonaceous aerosols over California based on satellite and ground observations, *J. Geophys. Res. Atmos.*, *118*, 11,148–11,160, doi:10.1002/jgrd.50835.

1. Introduction

[2] Black carbon, the main component of soot particles, is one of the largest contributors to global warming [*Jacobson*, 2010] through its light-absorbing effect. In addition to its direct warming effect, black carbon also influences cloud formation through its atmospheric heating and surface dimming [*Lau and Kim*, 2006; *Koch and Del Genio*, 2010] and by altering cloud microphysics through its ability to act as cloud condensation nuclei [*Nenes et al*., 2002]. Black carbon also influences large-scale climate indirectly by altering the spatial distribution of temperature and precipitation [*Menon et al*., 2002; *Chung and Ramanathan*, 2006].

[3] The incomplete combustion processes of fossil fuels (e.g., diesel engines), biofuels (e.g., firewood), and open biomass burning (e.g., wild fires) all produce carbonaceous aerosols [*Bond et al*., 2007] including both elemental carbon (EC) and organic carbon (OC) in the atmosphere. EC has long been shown to be a strong absorber of visible light [e.g., *Chylek et al*., 1984], and is therefore also referred to as black carbon (BC). From an observational perspective, the term "BC" is used for thermo-optical measurements while "EC" is used for optical filter measurements. Modelers also use "BC" as a generic term for highly absorbing, graphitized carbon [*Bond and Bergstrom*, 2006]. Several other studies have also pointed out the light absorption due to OC (in particular), suggesting the term "brown carbon" for OC [*Jacobson*, 1999; *Kirchstetter et al*., 2004; *Kanakidou et al*., 2005; *Andreae and Gelencsér*, 2006]. For simplicity and consistency in this paper, we use EC and OC to refer to the two main chemical species of carbonaceous aerosols. Recent studies largely based on in situ measurement show that OC is the largest contributor to the near-UV band absorption [e.g. *Barnard et al*., 2008; *Chakrabarty et al*., 2010; *Lack and Cappa*, 2010].

[4] The regional climate in California, in particular, may be sensitive to the radiative effect of carbonaceous aerosols

Additional supporting information may be found in the online version of this article.

[1]Scripps Institution of Oceanography, UC San Diego, California, USA.
[2]Atmospheric Science and Global Change Division, Pacific Northwest National Laboratory, Richland, Washington, USA.

Corresponding author: Y. Xu, Scripps Institution of Oceanography, UC San Diego, La Jolla, CA 92013, USA. (yangyang@ucsd.edu)

2169-897X/13/10.1002/jgrd.50835

because the summer water supply relies predominately on mountain snowmelt runoff, which is sensitive to EC surface deposition [*Hadley et al*., 2010] and the elevated warming. Studies also linked an observed increase in wildfire frequency in the Western US to warmer climate [*Westerling et al*., 2006], which may further amplify the concentration of carbonaceous aerosols. *Mao et al*. [2011] studied wild fires in the Western US using a chemical transport model and found the BC concentration simulated at high elevation regions are a factor of two lower than observations during summer fire seasons. *Myhre et al*. [2008] estimated the biomass-burning aerosol forcing using model-based approaches at regional scale of West Africa. Chemical transport models can simulate, in detail, the transport and deposition of aerosols in the atmosphere and are the main tools used to understand the loading and radiative impact of carbonaceous aerosols in the atmosphere [e.g., *Magi et al*., 2009; *Lynn et al*., 2007]. The modeling approaches are particularly helpful in assessing the sector contribution to radiative forcing and future projection based on specific control measures [*Koch et al*., 2007]. *Bond et al*. [2013] provided an in-depth assessment of BC radiative forcing largely based on modeling. However, such bottom-up models that rely on emission inventories can present large uncertainties as discussed by *Bond et al*. [2013], in which the bottom-up modeling results need to be further constrained by the observations to give a better estimate of BC radiative forcing at a global scale.

[5] In this study, we use a top-down approach that integrates ground observations, satellite observations, and model simulations to provide a comprehensive assessment of carbonaceous aerosol optical properties (including spectral dependency of aerosol optical depth and aerosol absorption optical depth (AAOD)) and radiative forcing over California. We discuss the methods in section 2. Then, we show the distribution of carbonaceous aerosol optical properties in section 3. Finally, we estimate the radiative forcing of EC and OC based on their integrated aerosol properties and compare these with available model output (section 4).

2. Methods

[6] The approach to estimating carbonaceous aerosol radiative forcing consists of three steps: (1) Creating an observationally integrated data set of aerosol physical and optical properties, including aerosol optical depth (AOD), aerosol absorption optical depth (AAOD) (section 2.1), and vertical profile (section 2.2). (2) Partitioning the total aerosol absorption into chemical species (EC, OC, and dust) based on a newly developed scheme (section 2.3). (3) Estimating the 3-D structure of radiative forcing (section 2.4).

2.1. Aerosol Optical Properties

[7] The data set used in this study originates from multiplatform observations of aerosol optical properties, notably AOD and AAOD. A larger AOD indicates a greater amount of aerosols existing in the atmospheric column, which, in turn, reduces the penetration of solar radiation toward the surface by scattering the light back to space and absorbing the energy. AAOD is the absorbing component of AOD and is directly related to the aerosol's warming potential. Both AOD and AAOD are wavelength dependent, and in this study, we focus on the visible band (about 400–700 nm). The AOD and AAOD are extensive properties, so the total AOD and AAOD can be roughly treated as the sum of AODs and AAODs from individual aerosol species (i.e., any nonlinearity arising from the aerosol mixing state is not taken into account).

[8] 1. AOD: The Aerosol Robotic Network (AERONET) is a global observation network of sun radiometers built to provide ground measurement of aerosol optical properties in an atmospheric column [*Holben et al*., 2001]. Twelve AERONET sites are located within California and neighboring states (Oregon, Nevada, and Arizona; Figure 3). The AOD data we used are the Level-2 (after cloud screening and quality control) all-points data set from 2000 to 2010 (Version 2). The all-points data were compiled into seasonal averages over individual stations. The seasonal climatological data were not compiled at stations where the data record was insufficient for 2000–2010. While AERONET provides high-accuracy, quality-controlled measurement of AOD, it cannot provide complete spatial coverage over the entire California domain because of the limited number of stations (Figure 3). For this reason, we also used satellite-observed AOD in this study.

[9] The Multi-angle Imaging Spectro Radiometer (MISR) on board NASA's Terra satellite has been providing decade-long monitoring of AOD measurement over the globe since 2000 [*Kahn et al*., 2010]. While we note that the Moderate Resolution Imaging Spectroradiometer (MODIS) aerosol product had greater spatial resolution and shorter revisit time, comparisons with AERONET long-term AOD measurements over California suggest that the MISR AOD product has better agreement than MODIS, particularly over bright desert surfaces [*Kahn et al*., 2009]. Another available long-term AOD data set from space is Sea-viewing Wide Field-of-view Sensor (SeaWIFS). This data set is not used in this study because it only provides AOD data for wavelengths shorter than 670 nm over land [*Hsu et al*., 2012], and the partitioning scheme we used to isolate carbonaceous aerosol AOD requires AODs at multiple wavelengths across the visible to near-infrared spectra (e.g., 440, 670, and 870 nm from MISR). We downloaded the 0.5 degree by 0.5 degree monthly averaged AOD data from MIST for the years 2000–2010. Validation of MISR AOD observations with ground-based AERONET and other satellite measurements has been done by numerous studies that show reasonably good agreement [*Kim and Ramanathan*, 2008; *Kahn et al*., 2010]. Figure 1a illustrates the 11 year averaged (2000–2010) annual mean AOD at 440 nm over California (with spatial resolution of 1 degree by 1 degree), showing aerosol climatology over this region with higher AOD along the coastal regions and Southern California inland.

[10] 2. SSA_AERONET: Single-scattering albedo (SSA) is defined as 1-AAOD/AOD, which has a range of 0 to 1 (with the limits of 1 corresponding to nonabsorbing and 0 corresponding to completely absorbing aerosols). SSA is an intrinsic property that is solely determined by the chemical composition and size distribution of the aerosol mixtures, rather than extrinsic property that is governed by the amount of aerosol mass loading. The total amount of visible light absorbed by EC is highly sensitive to the SSA, so the accurate estimate of SSA is crucial to quantifying the radiative forcing.

[11] Current SSA observations from MISR are not quality assured. Our analysis (not shown) suggests significant bias in California and other parts of the world. The Ozone

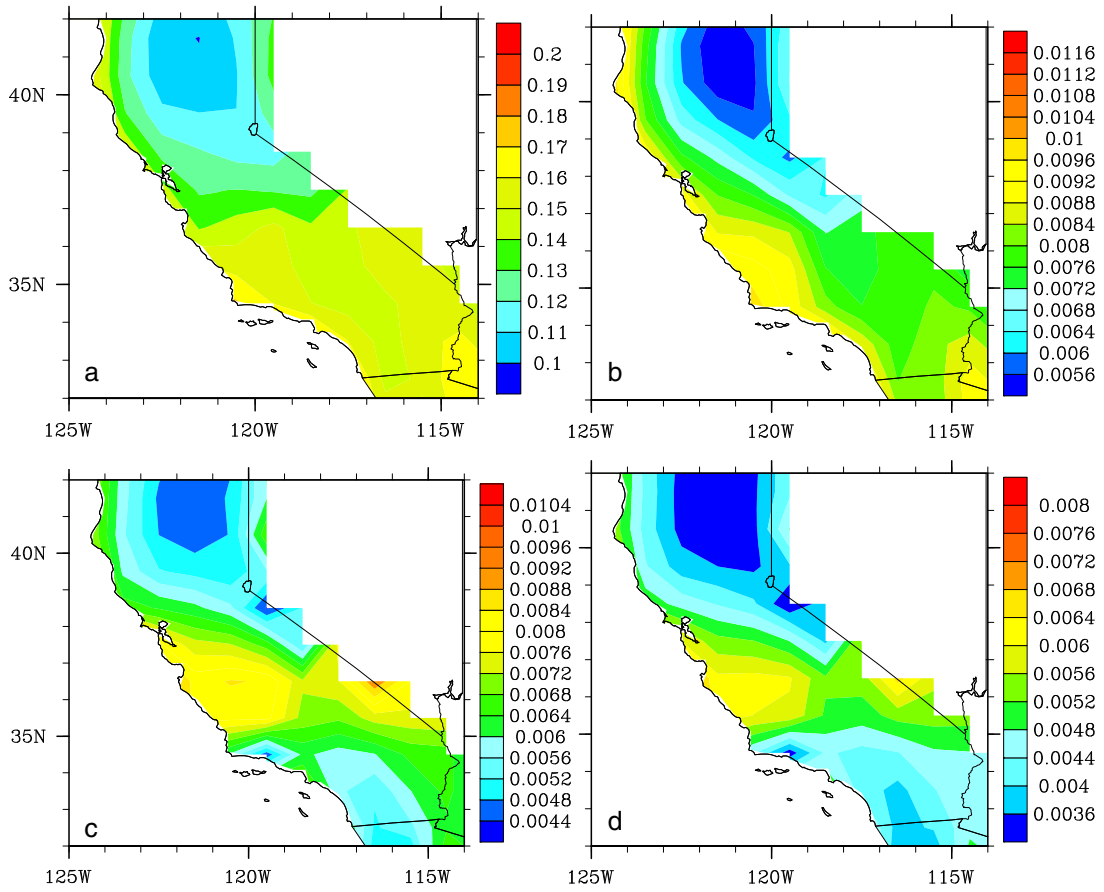

Figure 1. (a) Total AOD (440 nm). (b) Total AAOD (440 nm). (c) EC AOD. (d) EC AAOD. Estimates are based on MISR AOD and AERONET SSA. Spatial resolution of the integrated data set is 1 degree.

Monitoring Instrument (OMI) also has the capacity to measure SSA, but only at ultraviolet wavelengths [*Torres et al*., 2007]. SSA from OMI is useful in qualitatively distinguishing certain aerosol types [e.g., smoke, *Wilcox*, 2010], but does not provide sufficient spectral information to quantitatively calculate radiative forcing. Therefore, we did not utilize space-based SSA measurements or absorption-related information in this study. We hope that future deployment of advanced remote sensing techniques [e.g., the Glory Project's Aerosol Polarimetry Sensor; *Cairns et al*., 2010] may provide unprecedented continuous measurement of SSA from space.

[12] AERONET sites report AAOD and SSA from sky radiance measurements at 440, 675, 870, and 1020 nm only if the total AOD exceeds a threshold value of 0.4 at 440 nm. This condition must be satisfied to provide a high enough signal-to-noise ratio for the AERONET inversion algorithms. Because the total AOD over California is less than this threshold value (Figure 1a) most of the time, AERONET does not resolve the AAOD from the AOD—even that part of the AOD that is indeed contributed by aerosol absorption. To properly account for aerosol absorption, we therefore used all available AAOD measurements (and the simultaneous AOD measurements) from the AERONET all-points data set to calculate the SSA at high AOD events. We then applied the same SSA value to the low AOD measurements to calculate AAOD that were not directly reported. The assumption here is that SSA is an intrinsic property determined by chemical composition but not the total amount of aerosol. Therefore, in the event when the total amount of aerosol is insufficient for AERONET to retrieve SSA, SSA is assumed to be the same as the seasonal average calculated from the large AOD events. Note that at some sites, SSA_AERONET seasonal climatology was not available due to the absence of any high AOD period in certain seasons. The possibility that SSA may be biased and not universal is tested in Figures S3 and S4 of *Bahadur et al*. [2012], in which we showed the AERONET SSA as a function of AOD from various sites (not only limited to California and so with an even larger AOD span). The independence of SSA relative to AOD suggests that the bias of using SSA measurements at high AOD events to represent SSA at low AOD events is minimal.

[13] The seasonal mean values of AERONET SSA from each site were then summarized as average values for six regions of California. North is defined as area north of 38°N, Central being the area within 35°N–38°N, and South as area south of 35°N. Each region was further divided into "Coastal" for areas close to the coastline (about 200 km or two degrees) and "Inland" (200 km east of coastline) to account for the potential variation in aerosol composition arising from different emission sources. Such regional divisions are also recommended by air-pollution management agencies (e.g., California Air Resource Board's air basin divisions). The AAOD distribution suggests stronger aerosol absorption along the coastline (Figure 1b), which corresponds to patterns of human habitation in California. The caveat here is that AERONET SSA at sparsely located sites can cause bias when

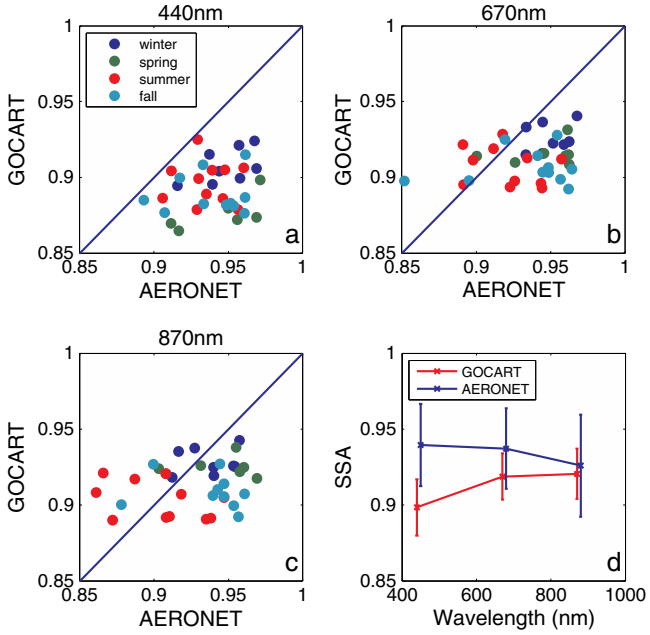

Figure 2. (a) Single-scattering albedo (SSA) seasonal averages from AERONET and GOCART at 440 nm. (b) At 670 nm. (c) At 870 nm. Each dot represents the seasonal average over one of the six California subdomains. Seasons are color coded. (d) Annual averages of SSA from AERONET and GOCART at three wavelengths. The error bars of Figure 2d represent the uncertainty due to seasonal and spatial variations of SSA.

used as a regional average. The potential sea-salt contamination in the AOD and AAOD record found in coastal sites is discussed in *Bahadur* [2012]. Given this situation, we sought an additional SSA data set for this study.

[14] 3. SSA_GOCART: Because the SSA obtained from AERONET measurements (denoted as SSA_AERONET) is limited in location and time (Figure S1), we also used output from the Goddard Chemistry Aerosol Radiation and Transport Model [GOCART; *Chin et al*., 2002] as the model-based alternative for SSA (denoted as SSA_GOCART). GOCART simulates aerosol components, including sulfate, dust, EC, OC, and sea-salt aerosols. The bottom-up chemical transport model takes emission of various aerosols and their precursors as input and simulates the reaction, transport, and deposition of chemical species under assimilated meteorological fields in order to predict atmospheric concentrations. Offline Mie code calculations are used to develop parameterizations for a mass extinction coefficient and a mass absorption coefficient (and associated SSA) as a function of refractive indices and size distribution and particle density. The chemical transport model then calculates the column optical properties from mass concentration using the parameterization scheme. The SSA_GOCART used in this study for total aerosol and individual aerosol species was calculated from GOCART output of AOD and AAOD for 2000–2007. We compared the seasonal mean SSA_GOCART with the SSA_AERONET at collocated sites. SSA_GOCART was smaller than SSA_AERONET at all three wavelengths, in particular over 440 nm (Figure 2).

[15] Possible reasons for the SSA discrepancy are:

[16] 1. The dust SSA at 440 nm in GOCART is about 0.83, which is significantly lower than the value of 0.91 we obtained from the observation-based approach [*Bahadur et al*., 2012]. Dust SSA of GOCART was based on refractive index and size-distribution assumptions ranging from 0.1 to 10 μm in radius over eight size groups, while the empirically derived dust we used was based on AERONET measurements from dust-dominated sites. GOCART may have overestimated dust absorption at 440 nm by assuming a lower SSA value. The overestimation of dust absorption was also reported over the Sahara Desert in another global aerosol model—the Module Aerosol Model 3 of *Ghan et al*. [2012]. Because dust AOD and AAOD decrease sharply with increasing wavelengths due to the large particle size, the discrepancy between modeled and observed SSA decreases with wavelength (Figure 2d).

[17] 2. The higher ratio of EC AOD versus total AOD simulated by GOCART may also have contributed to the overall lower SSA. The carbonaceous aerosol emission inventory used by GOCART is based on energy use and combustion technology of the early 1990s [*Cooke et al*., 1999]. *Bahadur et al*. [2011] suggested that diesel engine filter installation since the 1980s have significantly reduced the EC emissions of California by about 50%. Considering this EC emission reduction, GOCART results may overestimate present-day EC concentrations and therefore have a smaller SSA compared to the AERONET results.

[18] In summary, we currently find no additional available approach that can further constrain the "true" value of SSA and instead suggest that SSA inferred directly from AERONET observation and from GOCART model are likely limiting values (Figure 2d). Therefore, we calculated the aerosol properties and radiative forcing in two parallel cases (SSA_AERONET and SSA_GOCART) to bracket the uncertainty due to the imperfect data sources for SSA measurements. In other words, the SSA_GOCART estimates were considered as a hybrid method (AOD from observation and

SSA from modeling) to account for the limitations of the observational data set.

2.2. CALIPSO Vertical Profile of Aerosols

[19] Aerosols in the atmosphere are not well mixed and the vertical location of the aerosol layer is important for its radiative impact [*Koch and Del Genio*, 2010]. If the aerosols are above the cloud layer, their absorption tends to be enhanced [e.g., *Chylek and Coakley*, 1974] due to the higher albedo underneath the aerosol layer. If the scattering aerosol layer is located beneath cloud layer, its radiative effect is minimal. The Cloud-Aerosol Lidar and Infrared Pathfinder Satellite Observation (CALIPSO) satellite [*Young and Vaughan*, 2009] provides the aerosol extinction coefficient profile over the globe, which corresponds to the vertical distribution of aerosols and cloud. The CALIPSO Cloud and Aerosol Profile Products document reports on profiles of particle extinction and associated layer optical depths [*Young and Vaughan*, 2009]. The cloud and aerosol profile products are reported at a vertical resolution of 30 to 180 m and a horizontal resolution of 5 km. We calculated seasonal climatology using the data from summer of 2006 to spring of 2011 (day and night profile). The aerosol vertical profiles were generally similar across the seasons, showing an elevated aerosol layer at about 200 m (Figure S2). Winter and spring profiles exhibited elevated layers between the 1500 and 3000 m altitude ranges for Northern California (Figure S2a), which probably correspond to the long-range transport from Asia [*Hadley et al*., 2007]. The elevated dust signal (long-range transported) over Southern California (Figure S2) is not obvious, which suggests that the maximum dust AAOD for Southern California (Table 2) is more influenced by local dust sources (Mojave Desert and Anza-Borrego Desert, etc.) The observation of optical depth with boulder layer from CALIPSO can be problematic due to the topography and cloud contamination. Therefore, we adopted the surface extinction coefficient, which was directly measured at surface sites by Interagency Monitoring of Protected Visual Environments (IMPROVE) sites in California from 1988 to 2008 [*Chow et al*., 2001]. Averaged over multiple years and resolved into North/Central/South regions, the dominant aerosol layer is close to the surface (Figure S2). The seasonal mean profiles that combine CALIPSO and IMPROVE measurements over the North/Central/South regions were eventually used in the radiative forcing calculations. CALIPSO also provides qualitative aerosol type identification (i.e., mask feature), in which a layer is characterized by a dominating species. However, we note that even when an aerosol layer is classified as a certain aerosol type, there are still potentially various aerosol species mixed within that layer which could affect the forcing of individual species. Therefore, we did not use this species-dependent profile in our study.

2.3. Objective Method to Partition Aerosol Absorption

[20] After retrieving the total AOD and AAOD at multiple wavelengths over California (Figures 1a and 1b), we attempted to partition the total AOD and AAOD into different chemical species. In addition to EC, OC and dust also absorb solar radiation. While EC absorbs over the entire visible spectrum, OC and dust absorption are predominantly in the ultraviolet and near-ultraviolet spectra. The absorption Angstrom exponent (AAE) for EC, therefore, is much smaller than that for OC and dust. High values of OC AAE have been widely documented by many field studies [*Flowers et al*., 2010; *Gyawali et al*., 2009; *Moosmuller et al*., 2011], typically ranging from 3 to 5. Similarly, field studies concentrating on dust-dominated aerosols [*Fialho et al*., 2005; *Bergstrom et al*., 2007] report an AAE with large variability but typically in the range of 2 to 3 indicating enhanced absorption at shorter wavelengths. In contrast, very low values of AAE (less than 1.0) have been reported [e.g., *Clarke et al*., 2007; *Roden et al*., 2006; and *Yang et al*., 2009] in measurements containing urban air samples polluted by fossil fuel combustion. The wavelength dependence of absorption can, therefore, serve as a tool to distinguish different aerosol chemical species [*Russell et al*., 2010]. We recently developed a new empirical scheme to simultaneously partition the total AOD and AAOD into EC, OC, dust, and pure scattering aerosols [*Bahadur et al*., 2012]. The parameter values are based entirely on observations and therefore do not require the assumption of aerosol chemical and physical properties such as refractive index, mixing state, internal particle structure, or size distributions.

[21] 1. First, we empirically determined the representative AAE for EC, OC, and dust by exploiting the observed AAE from AERONET sites near source regions dominated by emissions associated with EC, OC, and dust (fossil fuels, biomass, and deserts, respectively). Dust aerosol sources are distinct from the combustion-related origin of carbonaceous aerosols and have significantly different wavelength dependencies of absorption and scattering. EC and OC are co-emitted from fossil-fuel-burning and biomass-burning sources. Because EC has a weaker spectral dependence than OC, we can posit that the lower end of the AAE values reflects absorption due to EC. We calculated the mean values of AAE by averaging the fractions of the total frequency distribution at the different AERONET sites and found that the mean AAE value asymptotically converges to 0.55 ± 0.24, a value representing the EC AAE. The OC AAE was determined (4.55) in a self-consistent manner by exploiting AAOD measurement from AERONET at the longer wavelengths of 870 and 1020 nm, with an additional assumption that OC has negligible absorption at those longer wavelengths. AAE2 that relates AAOD at 670 nm and 870 nm can be obtained similarly (Table 1).

[22] 2. Given the representative AAE of dust, EC, and OC (Table 1), we then solved the equation set (see equation 4 of *Bahadur et al*. [2012]) to simultaneously partition the total AAOD into those species (Table 2). In the partitioning scheme, we also consider the Angstrom exponent (AE) as an indicator of aerosol size. Compared with combustion aerosols that are predominantly in the fine mode, dust particles are dominated by coarse mode particles that have a weak spectral dependence for the total extinction (smaller AE). We therefore consider data points with AE smaller than 0.5 to be dust dominated and the absorption is completely attributed to dust.

[23] As a sensitivity test, we relax the criterion by considering data points with AE smaller than 0.8 to be dust dominated, in which case the total AAOD tends to be partitioned more toward dust (by more than two time over Northern California) and less toward EC and OC (by 5%–16%). We find over California region, such data points (at a 1 degree by 1 degree resolution) are not common, and according to the sensitivity test, the partitioning of AAOD in this study

Table 1. Comparison of Typical Values of SSA and AAE (Absorption Angstrom Exponent) Determined From AERONET by a Recursive Numerical Approach (*Bahadur et al*. [2012]) and in GOCART Simulations[a]

AERONET	AAE (440–670)	AAE2 (670–870)	SSA (440)	SSA (670)	SSA (870)
Dust	2.20	1.15	0.87	0.90	0.94
OC	4.55	--	0.77	0.80	1.00
EC	0.55	0.85	0.48	0.43	0.39
GOCART	**AAE (450–650)**	**AAE2 (650–900)**	**SSA (450)**	**SSA (650)**	**SSA (900)**
Dust	1.86	1.08	0.83	0.91	0.94
OC	0.46	−0.47	0.98	0.96	0.91
EC	1.18	1.13	0.25	0.18	0.11

[a]The AERONET-based AAE and SSA are adopted from *Bahadur et al*. [2012]. The AERONET-based SSA for each species is calculated at AERONET sites where each absorbing species is expected to be dominant. For example, EC SSA is determined from many fossil-fuel-dominated sites around the globe including Billerica (MA, USA), City College of New York (NY, USA), Fresno (CA, USA), Goddard Space Flight Center (MD, USA), Halifax (Canada), MD Science Center (MD, USA), Hamburg (Germany), Institute for Tropospheric Research Leipzig (Germany), Istituto per lo Studio delle Dinamica delle Grandi Masse (Italy), Mainz (Germany), Palaiseau (France), Rome (Italy), Hong Kong (China), Karachi (Pakistan), New Delhi (India), Taipei Central Weather Bureau (Taiwan), Kanpur (India).

is not likely to be affected much. However, cautions need to be taken when such a method is applied to areas possibly dominated by dust. More importantly, future field observations that have simultaneously chemical and optical measurement are needed to further verify and improve the method currently used, in particular regard to possible wide range of dust AAE.

[24] 3. SSA of EC, OC, and dust (Table 1) were also determined empirically with the single data set of AERONET, by a recursive numerical approach [*Bahadur et al*., 2012]. The AERONET-based SSA is calculated at AERONET sites where each absorbing species is expected to be dominant. For example, EC SSA is determined from many fossil-fuel-dominated sites around the globe (see the full list in Table 1). We found AERONET-based SSA for EC (0.43 to 0.48 at 550 nm) higher than that typically reported by measurements for aerosol particles generated in the laboratory (0.15 to 0.30), because AERONET SSA is based on ambient observations of atmospherically processed EC that may have contamination from internally and/or externally mixed OC. Note that AAOD partitioning in (1) is independent of SSA retrieval. The AOD of EC, OC, and dust were calculated backward from AAOD of those species (i.e., Figure 1c showing EC AOD). We consider the remaining fraction of total AOD as a contribution of scattering (i.e., nonabsorbing) aerosols including sulfates and nitrates. Details and validation of the scheme are discussed in *Bahadur et al*. [2012] and the supplemental materials therein.

2.4. Radiative Forcing Calculation

[25] The Monte Carlo Aerosol and Cloud Radiation transfer model (MACR) was initially designed and validated during the Indian Ocean Experiment (INDOEX) campaign [*Podgorny and Ramanathan*, 2001] and has been improved over the years and successfully applied in a number of global and regional aerosol studies [e.g., *Chung et al*., 2012; *Kim and Ramanathan*, 2012]. The model simulates energy flux from top to bottom of the atmosphere by tracing the movement of photons through 50 vertical layers with random processes, built upon the so-called Monte Carlo Independent Column Approximation approach [*Pincus et al*., 2003]. It includes diurnal and seasonal variation of solar zenith angles, aerosol-cloud configurations, and 25 spectral bands ranging from 0.25 to 5.0 micrometers to cover the solar spectrum. The advantage of the Monte Carlo approach for solving the radiative transfer equation is that it provides more accurate atmospheric flux values than those obtained with the two-stream approximations. MACR adopted the correlated k-distributions based on HITRAN 2000 database to incorporate gaseous absorption by water vapor, ozone, oxygen, and carbon dioxide [*Kato et al*., 1999].

[26] The scattering and absorption of clouds and aerosols are also taken into account. The total cloud amounts and cloud optical depths were obtained from Clouds and the Earth's Radiant Energy System [CERES; *Wielicki et al*., 1996] and subdivided into low, middle, and high cloud based on data from the International Satellite Cloud Climatology Project [ISCCP; *Rossow and Schiffer*, 1999]. Water particle radius and ice particle effective diameter are also provided by CERES and they are used for retrieving cloud single-scattering albedo (as a function of wavelength) and asymmetry factors using Optical Properties of Aerosols and Clouds (OPAC) software [*Hess et al*., 1998]. The ozone and water vapor concentrations were provided by OMI [OMDOAO3G data set; *Veefkind et al*., 2006]. The clear-sky surface albedo is provided by CERES. The various data sets are available at different spatial and temporal resolutions, but all were interpolated into 1 degree by 1 degree grids and seasonal averages before the MACR is deployed.

[27] In summary, the model input included: the integrated observation of AOD/AAOD at multiple wavelengths (section 2.1), partitioned AOD/AAOD and respective asymmetry factors for individual aerosol species (section 2.3), and the aerosol vertical profile (section 2.2). The sensitivity of calculated forcing toward input parameters (AOD, AAOD, SSA, asymmetry factor) has been tested by prior studies [*Chung et al*., 2012; *Kim and Ramanathan*, 2008]. The MACR model then simulates the energy flux at the 1 degree by 1 degree grids throughout the atmosphere to the surface. The difference in flux between two sets of simulations (one with specific aerosols and one without aerosols) yields the radiative forcing of the respective aerosol. We conducted similar calculations in

Table 2. Seasonal and Annual Averages of 550 nm AAOD of Dust, EC, and OC[a]

	Winter	Spring	Summer	Fall	Annual
Dust (North)	0.0003	0.0003	0.0002	0.0002	0.0002
Dust (Central)	0.0002	0.0003	0.0000	0.0006	0.0003
Dust (South)	0.0027	0.0029	0.0000	0.0012	0.0017
EC (North)	0.0038	0.0041	0.0038	0.0031	0.0037
EC (Central)	0.0042	0.0057	0.0058	0.0035	0.0048
EC (South)	0.0021	0.0040	0.0058	0.0038	0.0039
OC (North)	0.0009	0.0009	0.0009	0.0008	0.0009
OC (Central)	0.0005	0.0005	0.0012	0.0008	0.0007
OC (South)	0.0001	0.0000	0.0010	0.0010	0.0005

[a]Estimates are based on MISR AOD and AERONET SSA. Winter is Dec–Feb; spring is Mar–May; summer is Jun–Aug; fall is Sep–Nov. The North/Central/South domains are divided by 35°N and 38°N, as discussed in the text.

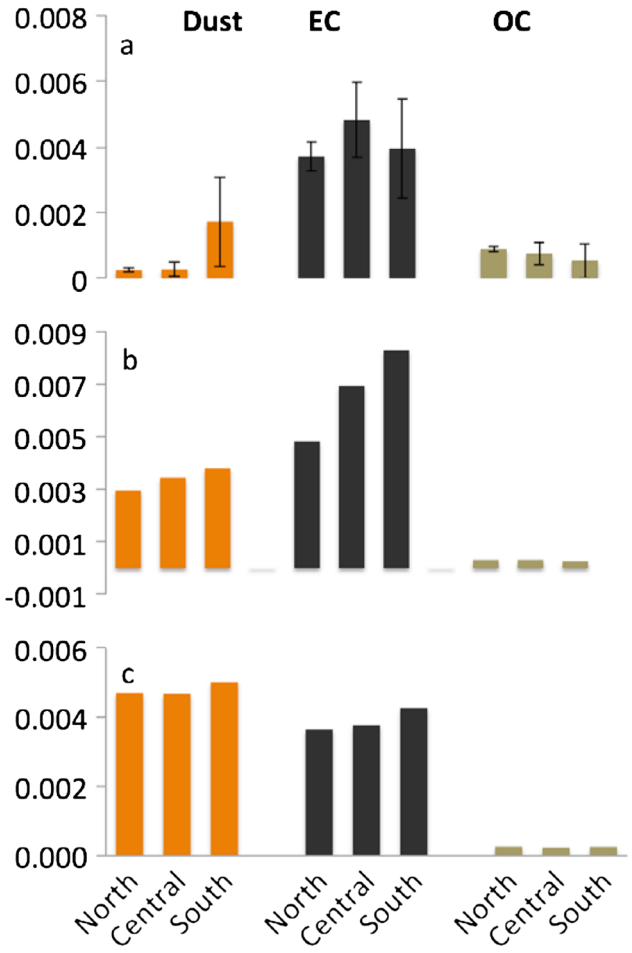

Figure 3. Climatological AAOD (550 nm) for dust, EC, and OC using different data set of (a) AOD from MISR, SSA from AERONET. (b) AOD from MISR, SSA from GOCART. (c) Output from GOCART climatological AAOD. Error bars represent the uncertainty due to seasonal variations.

the absence of clouds to obtain aerosol radiative forcing in clear-sky conditions.

3. Results and Discussion

3.1. Carbonaceous Aerosol Optical Properties

[28] Our first focus was to separate the AAOD contribution of carbonaceous aerosol (mainly due to anthropogenic sources) and natural dust aerosols. On average, the total AAOD at 440 nm over California was about 0.005–0.01, which is about 5% of the total AOD (Figure 1b). Southern California has larger AAOD than Northern California, which is consistent with its greater population density. The separation of the total AAOD into dust and carbonaceous aerosol suggests that the loading of dust is much higher in the southern region (Figure 3a), which is consistent with its drier climate and semi-desert environment. However, using the SSA values from the GOCART model (SSA_GOCART), such a north-south difference in dust loading was less significant (Figure 3b), but the overall dust loading was significantly larger in the SSA_GOCART estimate. Such a north-south difference was also missing in GOCART AAOD (Figure 3c), which is the direct output of GOCART model without using any observational constraint or partitioning scheme. From our observationally constrained estimates, carbonaceous aerosols contributed to the majority of the total AAOD, which was about four or five times larger than the dust AAOD at 550 nm (Figure 3a). The AAOD due to carbonaceous aerosols (EC and OC) at 440 nm was 50%–200% larger than natural dust. In the case of SSA_GOCART, the carbonaceous aerosol still dominated the AAOD, but the dust contribution was significantly larger and about 30%–70% of carbonaceous aerosol. Also, the total AAOD was larger in the SSA_GOCART estimates due to the fact that SSA from GOCART has smaller values (as discussed in section 2.2). The discrepancy in the AAOD partitioned from the SSA_GOCART and SSA_AERONET cases can be attributed to the essence of our partitioning method, which was to exploit the wavelength dependence of AAOD. Pure dust SSA in our calculation is assumed to increase with wavelength (from 0.87 at 440 nm to 0.90 at 670 nm), while EC SSA is assumed to decrease with wavelength (from 0.48 at 440 nm to 0.43 at 670 nm, Table 1). Since the total SSA_AERONET slightly decreased with wavelength (Figure 2d), which is similar to the EC AAOD wavelength dependence, our partitioning scheme tends to attribute a larger fraction of AAOD to EC and smaller fraction of AAOD to dust. The opposite applies to the case of SSA_GOCART. The current limitation of multiple-wavelength measurement of SSA is the fundamental reason that we cannot further reduce the difference between the two cases.

[29] We further assessed the relative contribution of AAOD from EC and OC. The partition based on SSA_AERONET suggested that OC AAOD was about 30%–50% of EC at 440 nm, dropping to only 15% at 550 nm (Figure 3a). On the other hand, partitioning based on SSA_GOCART (Figure 3b) suggests a much smaller OC contribution to AAOD, presumably because the model does not fully take into account the amount of OC absorption. The OC SSA for GOCART was 0.98 at 450 nm, in contrast to 0.71 obtained from the empirical approach used in this study. The EC AAOD in SSA_GOCART was larger than in SSA_AERONET because the total AAOD is larger in SSA_GOCART. This discrepancy of OC absorption in the two cases clearly indicates the need for further studies from observations and modeling to clarify this issue. EC AOD and AAOD are mainly concentrated in population-dense areas (Figures 1c and 1d), including the Bay Area, Central Valley, and Los Angeles metropolitan region. The AAOD of EC is relatively lower over the Southern California inland region (compare Figure 1d with Figure 1b) where dust aerosol originating in the desert regions appears to be the main absorber for Southern California.

[30] EC AAOD was largest in summer (0.006 at 550 nm for Central and Southern California), which might have been linked to wildfire activities [*Westerling et al.*, 2006]. The larger OC AOD value in summer and fall, especially over Central and Southern California, and the corresponding pattern of biomass-burning emission (Figure S3) seem to support this linkage. The seasonal variation of EC and OC is not entirely clear (Table 2). Most carbonaceous aerosol emissions in California are from anthropogenic activities, which do not exhibit obvious seasonal variation (see section 3.2 for details).

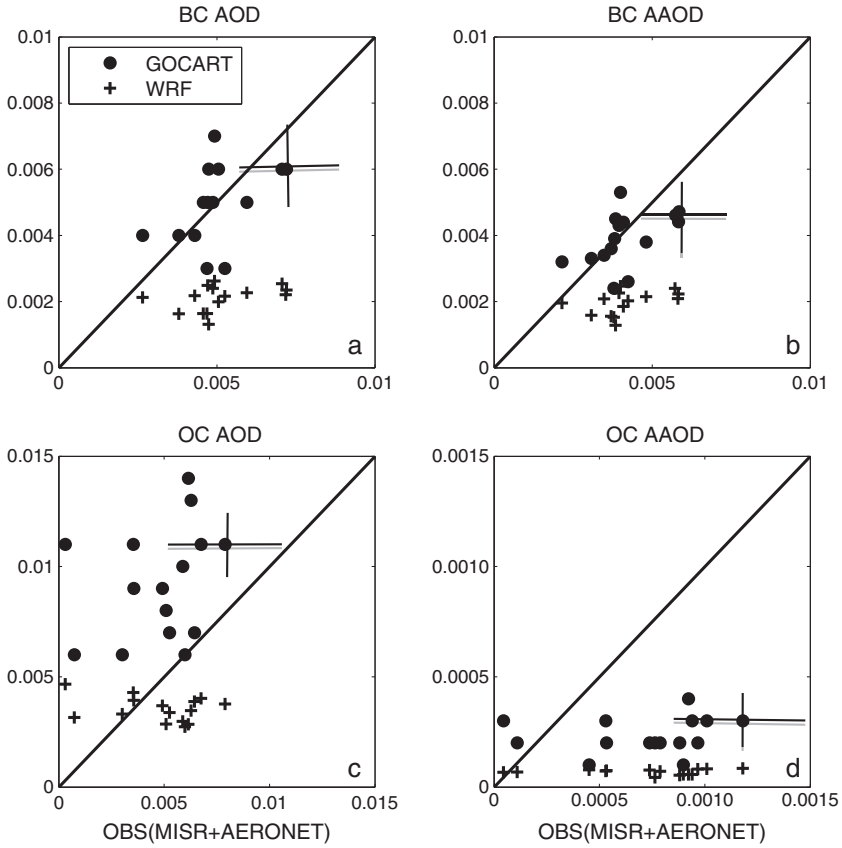

Figure 4. (a) EC AOD (550 nm) at different seasons and regions (Northern, Central, and Southern California) from pure observation method (OBS(AOD_MISR + SSA_AERONET)), compared with GOCART and WRF_Chem simulations (with standard EC emission). (b)–(d), same as Figure 4a, but for EC AAOD, OC AOD, and OC AAOD, respectively. The whiskers represent standard deviation of GOCART and OBS data due to seasonal and spatial variation. The magnitude of EC and OC AOD in the WRF_Chem simulation with standard emission is smaller than GOCART but also shows at least 200% variation. The OC AAOD of the WRF_Chem simulation is close to zero and without much variation due to the neglect of OC absorption in the WRF_Chem radiative transfer scheme.

[31] We compared the AOD and AAOD estimates with direct output of GOCART. Simulations from GOCART [*Chin et al*., 2002] from 2000 to 2007 were resolved into North/Central/South California and seasonally averaged to provide a point of comparison. The EC AAOD showed reasonably good agreement between GOCART and observations. The OC AAOD was underestimated by at least half, despite the fact that OC AOD was overestimated. The GOCART model presumes OC SSA to be 0.98 at 450 nm, while the empirical approach used in this study suggests OC SSA to be 0.71. The absolute values of AOD and AAOD for the SSA_GOCART case were different, but the seasonal trends as discussed above remained essentially the same. This suggests that, at least qualitatively, GOCART has the proper chemical mechanism and successfully captures the influence of meteorological conditions on aerosol transport and distribution.

[32] We also simulated carbonaceous aerosol with the model known as the Weather Research and Forecasting Model (WRF_Chem) Coupled with Chemistry [*Grell et al*., 2005]. The WRF_Chem model was specifically configured at high spatial resolution (12 km) for the California region to better resolve the complex orography [*Zhao et al*., 2013] and includes a more updated emission inventory produced by the California Air Resources Board [*CARB*, 2008] with much finer spatial resolution than GOCART. We found that the EC AOD and AAOD simulated by WRF_Chem with the standard CARB emission inventory were 50% lower than both GOCART and the observational estimates (Figures 4a and 4b). This could be due to a potential underestimation in the EC emissions, which were based on measurements from a 2 week period in 2008 during the CARB Arctic Research of the Composition of the Troposphere from Aircraft and Satellites (ARCTAS) campaign. Therefore, we also ran WRF_Chem simulations that doubled the EC emission inventory (Table 3). The simulated EC surface concentration shows better agreement compared with ground observations when EC emissions are doubled [*Zhao et al*., 2013]. The WRF_Chem-simulated OC AOD was comparable with observational estimates, but simulated OC AAOD was virtually zero (Figure 4), as the model does not take into account any OC absorptions in the radiation code. The negligible OC AAOD simulated by WRF_Chem is a result of the enhancement of absorption when OC is internally mixed with EC, rather than from direct absorption by OC itself. On the other hand, in the observational estimates, this kind of nonlinearity arising from the aerosol mixing state is not taken into

Table 3. Top-of-Atmosphere (TOA) and Atmospheric (Atm) Forcing (W/m^2) of EC and OC Estimated From Two Methods (AOD_MISR + SSA_AERONET and AOD_MISR + SSA_GOCART) and Two Sets of WRF_Chem Simulation Results Using Different EC Emission[a]

	AOD_MISR + SSA_AERONET	AOD_MISR + SSA_GOCART	WRF_Chem (1*EC)	WRF_Chem (2*EC)
TOA EC (North)	0.28 (0.09, 0.46)	0.29 (0.12, 0.62)	0.21	0.29
TOA EC (Central)	0.49 (0.26, 0.95)	0.63 (0.24, 1.50)	0.32	0.47
TOA EC (South)	0.92 (0.37, 1.45)	1.93 (0.62, 3.98)	0.38	0.56
TOA EC (California)	0.56 (0.26, 0.95)	0.95 (0.35, 2.03)	0.30	0.44
TOA OC (North)	−0.08 (−0.17, −0.03)	−0.01 (−0.11, 0.13)	−0.12	−0.12
TOA OC (Central)	−0.06 (−0.16, 0.08)	−0.14 (−0.27, −0.03)	−0.15	−0.15
TOA OC (South)	−0.04 (−0.13, 0.07)	−0.01 (−0.16, 0.14)	−0.16	−0.16
TOA OC (California)	−0.06 (−0.11, 0.02)	−0.05 (−0.1, −0.02)	−0.14	−.14
Atm EC (North)	1.25 (0.71, 1.82)	1.72 (0.69, 3.82)	0.57	0.78
Atm EC (Central)	1.99 (1.04, 2.83)	2.68 (1.05, 5.95)	0.81	1.20
Atm EC (South)	2.11 (0.84, 3.39)	4.03 (1.45, 8.08)	0.93	1.37
Atm EC (California)	1.78 (0.86, 2.68)	2.81 (1.06, 5.95)	0.77	1.12
Atm OC (North)	0.47 (0.22, 0.69)	0.07 (0.01, 0.20)	0.03	0.03
Atm OC (Central)	0.41 (0.08, 0.76)	0.10 (0.01, 0.37)	0.05	0.05
Atm OC (South)	0.33 (0.02, 0.71)	0.02 (0, 0.47)	0.04	0.04
Atm OC (California)	0.40 (0.11, 0.72)	0.06 (0.01, 0.35)	0.04	0.04

[a]Atm forcing is calculated from the difference between TOA and surface forcing. "North"/"Central"/South" domains are divided by 35°N and 38°N, as discussed in the text; and "California" is the statewide average. Uncertainty due to seasonal variations for observation-based estimates is shown in brackets.

account. This neglect of OC absorption will have consequences regarding the radiative forcing, as discussed next.

3.2. Radiative Forcing

[33] The radiative forcing attributed to a certain type of aerosol is defined as the energy flux change when that type of aerosol is added into the clean atmosphere. Note that the radiative forcing discussed in this study is the aerosol direct forcing, and any potential impact of the aerosol on clouds is not considered in the model. Nevertheless, an accurate estimation of direct forcing of aerosol and its historical evolution is a key to understanding observed climate change phenomena in California. Table 3 summarizes the direct forcing at the top of the atmosphere (TOA), at the surface level (Sfc), and within the atmospheric column (Atm) averaged over Northern/Central/Southern California.

[34] According to our observational estimates, the atmospheric heating due to absorption by EC and OC was 1.7–2.4 W/m^2 (Table 3 and Figure 5). The GOCART simulation yielded atmospheric heating that was larger than the observational estimates by 30%, and this was consistent with the AAOD comparison (Figure 4b). GOCART, due to its coarser resolution (2.5 degree), was not able to capture the finer spatial variation (coast-to-inland, north-to-south) in our observational estimates (i.e., 1 degree). In contrast, WRF_Chem—with much finer spatial resolution—was capable of capturing the high concentration hotspot close to cities (Figure 5c).

[35] The TOA forcing due to carbonaceous aerosols ranges from 0.2 to 1.9 W/m^2 over California (see Table 3 for the uncertainty range due to seasonal and spatial variation). The annual mean and statewide average is 0.7 W/m^2 (0.5 to 0.9 considering uncertainty due to data source selection, Table 3). The positive value indicates that carbonaceous aerosol is a considerably large warming source at regional scales (note that the global average CO_2 warming is about 1.7 W/m^2). In contrast, dust aerosols had cooling effects at TOA, especially over Southern California, by 1.0–1.5 W/m^2 (Figure S4). The TOA forcing of carbonaceous aerosol also showed a north-to-south asymmetry, potentially associated with population and industrial activity differences between Northern and Southern California. The carbonaceous aerosol TOA forcing calculated from the WRF_Chem output was much smaller (−0.1–0.7 W/m^2), because OC forcing was more negative (−0.3 W/m^2). The large overall positive value of carbonaceous aerosol forcing obtained based on observation, in contrast with the WRF_Chem simulations, suggests that the OC scattering effect can largely offset the co-emitted EC's heating effect. Based on the observationally constrained estimates (SSA_AERONET and SSA_GOCART case), OC TOA forcing was close to zero (Table 3) due to the weak OC absorption, and therefore carbonaceous aerosol forcing was almost equal to the EC forcing (Figure 6). More importantly for the regional climate, the carbonaceous aerosols intercepted heat that would have reached the ground level and then induced atmospheric heating. The existence of carbonaceous aerosol reduces the solar radiation reaching the ground by 1.5–2.5 W/m^2. Such a dimming effect has climatic consequences in the water budget as it suppresses evapotranspiration from the surface [*Ramanathan et al*., 2001].

[36] Our calculation shows that EC's heating effect is about 75%–85% of the atmospheric heating from carbonaceous aerosol. OC absorption at 440 nm was as much as 30–50% of the EC absorption (Figure 3); but as OC absorption declined strongly toward the larger wavelengths, EC dominated the overall heating effect. Similar to the regional variation in AAOD shown in Figure 3, EC atmospheric heating was larger in Southern California, while OC was larger in Northern California; and both the pattern of spatial variation and the magnitude of EC atmospheric heating were also shown by the GOCART simulation (Table 3). The surface dimming effect of EC was about two to four times larger than that of OC. The estimation from SSA_GOCART showed even larger dimming contributed by EC and smaller dimming contributed by OC. Surface dimming from the GOCART output generally agreed with the observational estimates. Furthermore, GOCART also captured the larger forcing feature over Southern California. The observation-based estimate also showed high loading over Central

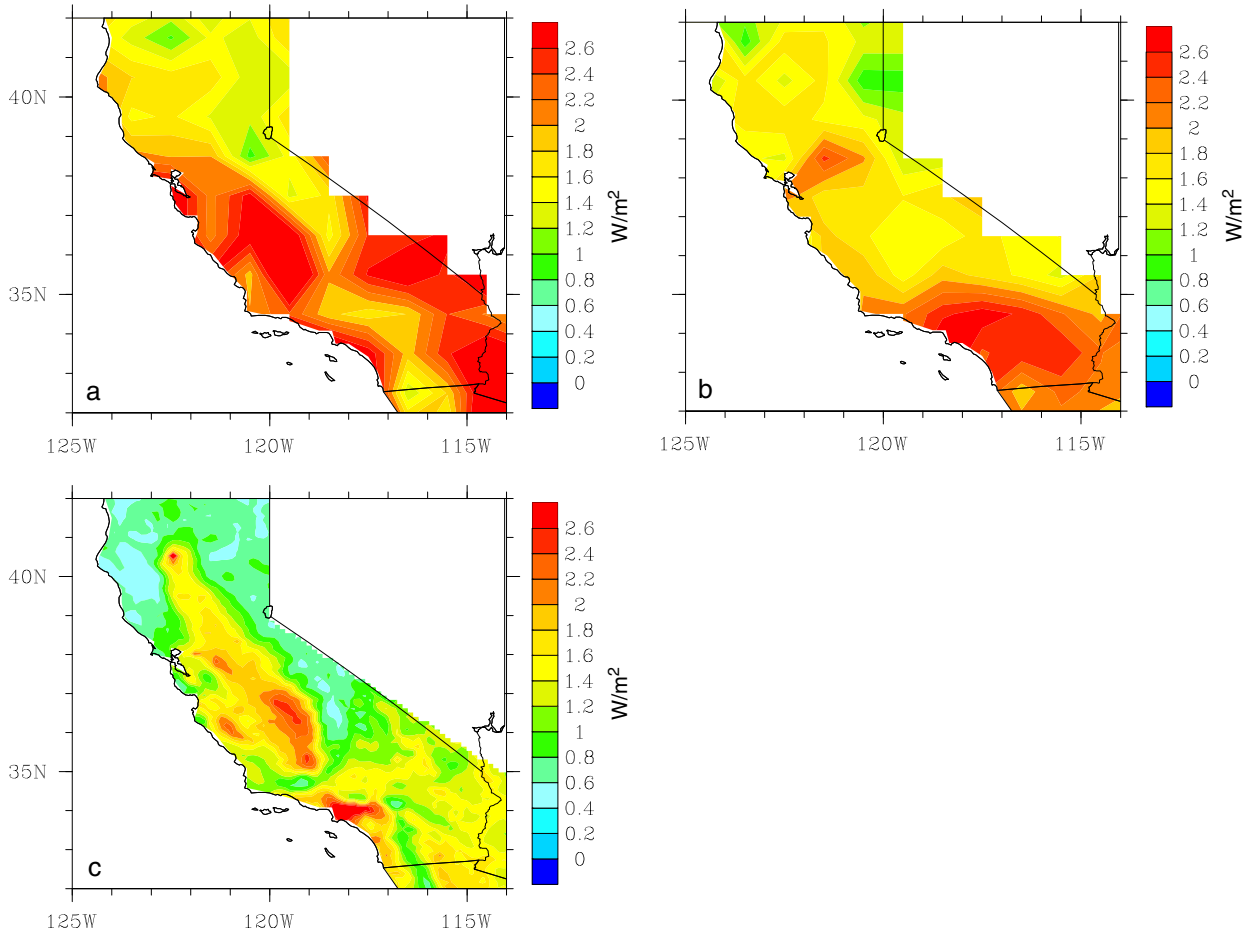

Figure 5. Annual mean of carbonaceous aerosol (EC + OC) atmospheric heating over California (W/m^2). (a) Observational estimates (AOD_MISR + SSA_AERONET). (b) GOCART simulation output. (c) WRF_Chem simulation with doubled CARB EC emission.

California, and WRF_Chem—with its finer spatial resolution—also captured the emission sources over the Central Valley regions (Figure 5).

3.3. Understanding the Model Bias

[37] Note that the AOD and AAOD intercomparison (Figure 4) and more detailed comparisons with IMPROVE and AERONET data [*Zhao et al.*, 2013] indicate that the WRF_Chem simulation with the standard CARB emission inventory underestimated EC surface concentration by at least a factor of two. The WRF_Chem estimated forcing shown here (Figure 5c) is from the simulation in which the standard EC emission was doubled. Despite this, the atmospheric forcing simulated by WRF_Chem is still smaller than the observational estimates by 15–30% (Table 3). Note that the WRF_Chem simulation was based on 2005 meteorology and 2008 emissions, while the observational estimate was for 2000–2010. The interannual variability of both emissions and meteorology may also contribute to the difference. In addition, the large difference in the California averaged forcing between observations and WRF_Chem is partly due to the large spatial gradients in heating simulated by WRF_Chem compared to the much smoother spatial patterns in the observational and GOCART estimates. The smoothed AOD/AAOD from the satellite estimates (as in Figure 1) have been validated with AERONET at the measurement sites. However, such measurements are not available for vast remote areas (Figure S1).

[38] In addition to uncertainty with data sources, we speculate that some remaining discrepancy is due to both

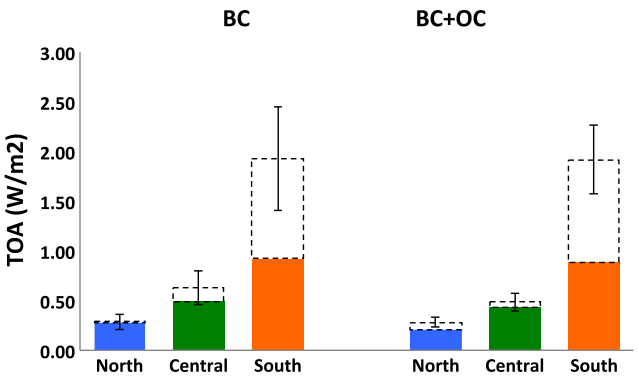

Figure 6. TOA forcing climatology due to (left) EC and (right) EC + OC. Solid: Observational estimates (AOD_MISR + SSA_AERONET). Dashed: Hybrid estimates (AOD_MISR + SSA_GOCART). Error bars represent the uncertainty due to spatial variation of forcing.

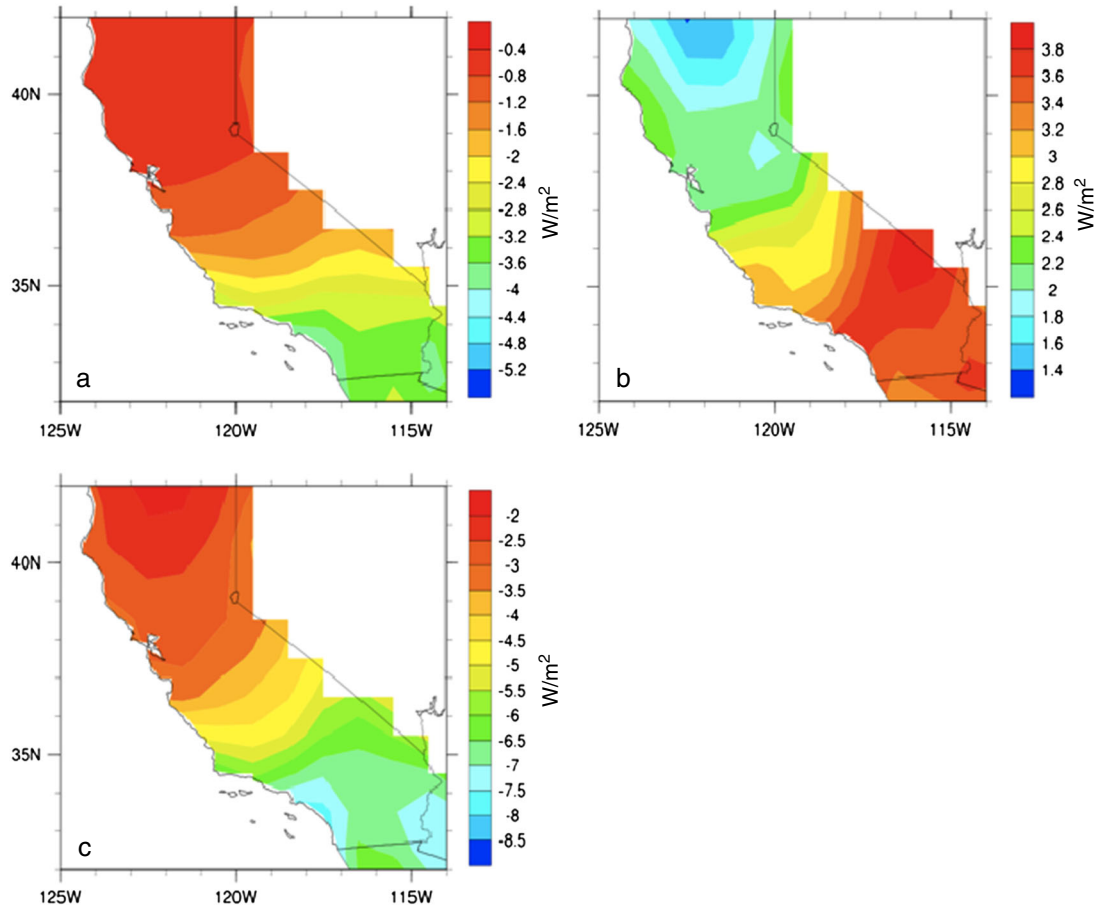

Figure 7. (a) TOA cooling (negative sign), (b) surface brightening (positive sign), and (c) atmospheric cooling (negative sign) (W/m^2) due to the 50% EC emission reduction during the last two decades.

emission inventory bias and the omission of OC absorption in the model. A new comprehensive report [*Bond et al.*, 2013] also identified that the emission inventory is almost globally biased with major biases over Africa and Asia. Here we wish to highlight that the OC TOA forcing is a small negative value according to our estimates (from 0.1 to 0 W/m^2), as the scattering effect of OC is partially offset by its relatively weak absorption. The TOA cooling effect of OC simulated by GOCART, in contrast, is three times larger than our estimates (-0.3 W/m^2). However, we point out that the uncertainty associated with the selection of SSA sources is at least 50% (dashed bars in Figure 6), and this uncertainty covers most of the discrepancy between the models. Compared to SSA_GOCART, the calculations using SSA_AERONET have a stronger OC absorption (also suggested by AAOD in Figure 3).

[39] The bias in OC absorption simulated by GOCART and WRF_Chem (Figure 5c) suggests that current model parameterizations are not able to fully capture the real OC absorption. Although it is negligible at long wavelengths, it comprises up to 50% of the EC absorption at short wavelengths, indicating that treatment of OC as absorbing is critical for successful estimations of aerosol forcing. The OC absorption is likely missing in many other climate models [e.g., *Koch et al.*, 2007; *Myhre et al.*, 2008] and that the models need to be further improved to incorporate the new experimental evidence of OC absorption. The inclusion or enhancement of OC absorption in the models has several consequences in our understanding of the radiative forcing of carbonaceous aerosols. For example, in areas where aerosol emission is greatly influenced by wildfire events (i.e., Africa, Amazonia, South East Asia) or by biofuel-burning (i.e., India), the overall radiative forcing contributed by carbonaceous aerosols may have been underestimated by previous models, as those models treat OC as a nonabsorbing species. Therefore, even models that accurately simulate the atmospheric loading of OC will not yield the correct magnitude for the radiative effect of OC. If the OC loading is sufficiently realistic, underestimation of OC absorption effects can even reverse the sign of carbonaceous aerosol TOA forcing from warming to cooling.

3.4. Surface Brightening Due to EC Emission Control

[40] As recently reported by *Bahadur et al.* [2011] using IMPROVE measurements, EC loading in California declined by 50% between 1980 and 2000, while no trends were seen for other aerosols. Such an effect was attributed to the effectiveness of air pollution control measures that specifically targeted emission from diesel combustion sources and domestic wood burning [*CARB*, 2008; *Kirchstetter et al.*, 2008]. We have also performed calculations that demonstrate the radiative forcing impact of such a 50% EC reduction (Figure 7). EC emission reduction during the last two decades leads to cooling of 0.8–3 W/m^2 at TOA. The

atmospheric cooling due to EC reduction was as large as 6 W/m^2 over Southern California. Another consequence of preferentially removing EC from the atmosphere was a surface brightening of 1.5–3.5 W/m^2. Such a brightening signal, if detected in the observation record, can provide an objective confirmation of the magnitude of forcing estimates and historical trends. The important inference we can make from the overall positive TOA forcing is that environmental protection activities in California targeting EC pollutants (and co-emitted OC) have effectively contributed to the mitigation of global warming.

4. Conclusions

[41] Our study utilizes multiple data sources including AERONET, MISR, GOCART, CALIPSO, and IMPROVE to construct a 3-D picture of aerosol over California from 2000 to 2010. Using a newly developed scheme, we partitioned the total aerosol absorption into EC, OC, and dust aerosols. The absorption of carbonaceous aerosol was larger than natural dust absorption, suggesting that anthropogenic activities play a major role in emitting absorbing aerosol. A large fraction of atmospheric heating was contributed by EC, with OC contributing the remaining 15%–25%. EC features a larger concentration over Southern California, while larger OC distribution is found over Northern California. We compared our calculations against the output from two chemical transport models (GOCART and WRF_Chem), and found reasonable agreement of EC absorption with these models. However, GOCART underestimates the OC absorption at least by 50%; WRF_Chem treats OC as purely scattering and significantly underestimates OC's absorbing ability.

[42] Our estimated TOA warming due to carbonaceous aerosols was 0.5–0.9 W/m^2 for the first decade of the 21st century. We also found that a weaker cooling effect was due to OC (smaller than -0.1 W/m^2) as compared with the models, as we treated OC to be absorbing in the near-UV band. The overall dimming effect of carbonaceous aerosol was about 1.5–2 W/m^2. This suggests that the solar radiation reaching the surface has increased by about 2 W/m^2 during the last two decades as a result of California air pollution regulations that track trends in aerosol species [*Bahadur et al*., 2011]. The observation-based estimates served as an independent result that verifies the performance of chemistry transport models in simulating the concentration and radiative effect of aerosols. One major implication from our analysis here is that current models (possibly with biased emission inventory and lack of treatment of OC absorption) may overestimate the TOA cooling effects from OC and therefore underestimate the overall warming effect from carbonaceous aerosols (i.e., co-emitted EC and OC), in particular over biomass-burning regions.

[43] **Acknowledgments.** This work was supported by California Air Resources Board (CARB) under contract 08-323, National Science Foundation (NSF) under award ATM 0721142, and by the Office of Science of the U.S. Department of Energy as part of the Regional and Global Climate Modeling program. The Pacific Northwest National Laboratory is operated for DOE by Battelle Memorial Institute under contract DE-AC05-76RL01830. We acknowledge Prof. V. Ramanathan for his valuable comments on the work. We also thank D. Kim, P. S. Praveen, T. Ahmed, B. Chen, J. Burney, and D. Biasca for their help during various stages of this project. The NASA AERONET group and GES DISC Giovanni system provided some data sets used in this study. We are grateful to four anonymous reviewers for their valuable comments that greatly improved the presentation of the work.

References

Andreae, M. O., and A. Gelencsér (2006), Black carbon or brown carbon? The nature of light-absorbing carbonaceous aerosols, *Atmos. Chem. Phys.*, *6*, 3131–3148.

Bahadur, R., Y. Feng, L. M. Russell, and V. Ramanathan (2011), Impact of California's air pollution laws on black carbon and their implications for direct radiative forcing, *Atmos. Environ.*, *45*, 1162–1167.

Bahadur, R., P. S. Praveen, Y. Xu, and V. Ramanathan (2012), Solar absorption by elemental and brown carbon determined from spectral observations, *Proc. Natl. Acad. Sci. U. S. A.*, *109*(43), 17,366–17,371, doi:10.1073/pnas.1205910109.

Barnard, J. C., R. Volkamer, and E. I. Kassianov (2008), Estimation of the mass absorption cross section of the organic carbon component of aerosols in the Mexico City Metropolitan Area, *Atmos. Chem. Phys.*, *8*, 6665–6679, doi:10.5194/acp-8-6665-2008.

Bergstrom, R. W., P. Pilewskie, P. B. Russell, J. Redemann, T. C. Bond, P. K. Quinn, and B. Sierau (2007), Spectral absorption properties of atmospheric aerosols, *Atmos. Chem. Phys.*, *7*, 5937–5943, doi:10.5194/acp-7-5937-2007.

Bond, T. C., E. Bhardwaj, R. Dong, R. Jogani, S. Jung, C. Roden, D. G. Streets, and N. M. Trautmann (2007), Historical emissions of black and organic carbon aerosol from energy-related combustion, 1850–2000, *Global Biogeochem. Cycles*, *21*, GB2018, doi:10.1029/2006GB002840.

Bond, T. C., and R. W. Bergstrom (2006), Light absorption by carbonaceous particles: An investigative review, *Aerosol Sci. Technol.*, *40*(1), 27–67, doi:10.1080/02786820500421521.

Bond, T. C., et al. (2013), Bounding the role of black carbon in the climate system: A scientific assessment, *J. Geophys. Res. Atmos.*, *118*, 5380–5552, doi:10.1002/jgrd.50171.

Cairns, B., M. Mishchenko, H. Marring, B. Fafaul, and S. Pszcolka (2010), Accurate monitoring of terrestrial aerosols and total solar irradiance: the NASA Glory mission, *Proc. SPIE*, *7826*, 78260U, doi:10.1117/12.865013.

California Air Resource Board (2008), Emission Inventory Data, http://www.arb.ca.gov/ei/emissiondata.htm.

Cooke, W. F., C. Liousse, H. Cachier, and J. Feichter (1999), Construction of a 1°*1° fossil fuel emission data set for carbonaceous aerosol and implementation and radiative impact in the ECHAM4 model, *J. Geophys. Res.*, *104*(D18), 22,137–22,162.

Chakrabarty, R. K., H. Moosmüller, L.-W. A. Chen, K. Lewis, W. P. Arnott, C. Mazzoleni, M. K. Dubey, C. E. Wold, W. M. Hao, and S. M. Kreidenweis (2010), Brown carbon in tar balls from smoldering biomass combustion, *Atmos. Chem. Phys.*, *10*, 6363–6370, doi:10.5194/acp-10-6363-2010.

Chin, M., P. Ginoux, S. Kinne, B. N. Holben, B. N. Duncan, R. V. Martin, J. A. Logan, A. Higurashi, and T. Nakajima (2002), Tropospheric aerosol optical thickness from the GOCART model and comparisons with satellite and sunphotometer measurements, *J. Atmos. Sci.*, *59*, 461–483.

Chow, J. C., J. G. Watson, D. Crow, D. H. Lowenthal, and T. Merrifield (2001), Comparison of IMPROVE and NIOSH carbon measurements, *Aerosol Sci. Technol.*, *34*(1), 23–34.

Chung, C. E., and V. Ramanathan (2006), Weakening of North Indian SST gradients and the monsoon rainfall in India and the Sahel, *J. Clim.*, *19*, 2036–2045.

Chung, C. E., V. Ramanathan, and D. Decremer (2012), Observationally constrained estimates of carbonaceous aerosol radiative forcing, *Proc. Natl. Acad. Sci. U. S. A.*, *109*(29), 11,624–11,629, doi:10.1073/pnas.1203707109.

Chylek, P., and J. Coakley (1974), Aerosol and climate, *Science*, *183*, 75–77.

Chylek, P., V. Ramaswamy, and R. J. Cheng (1984), Effect of graphitic carbon on the albedo of clouds, *J. Atmos. Sci.*, *41*, 3076–3084.

Clarke, A., et al. (2007), Biomass burning and pollution aerosol over North America: Organic components and their influence of spectral optical properties and humidification response, *J. Geophys. Res.*, *112*, D12S18, doi:10.1029/2006JD007777.

Fialho, P., A. D. A. Hansen, and R. E. Honrath (2005), Absorption coefficients by aerosols in remote areas: A new approach to decouple dust and black carbon absorption coefficients using seven-wavelength aethalometer data, *J. Aerosol Sci.*, *36*(2), 267–282.

Flowers, B. A., M. K. Dubey, C. Mazzoleni, E. A. Stone, J. J. Schauer, S.-W. Kim, and S. C. Yoon (2010), Optical-chemical-microphysical relationships and closure studies for mixed carbonaceous aerosols observed at Jeju Island; 3-laser photoacoustic spectrometer, particle sizing, and filter analysis, *Atmos. Chem. Phys.*, *10*, 10,387–10,398.

Ghan, S. J., X. Liu, R. C. Easter, R. Zaveri, P. J. Rasch, J.-H. Yoon, and B. Eaton (2012), Toward a minimal representation of aerosols in climate models: Comparative decomposition of aerosol direct, semidirect, and

indirect radiative forcing, *J. Clim.*, *25*, 6461–6476, doi:10.1175/JCLI-D-11-00650.1.

Grell, G. A., S. E. Peckham, R. Schmitz, S. A. McKeen, G. Frost, W. C. Skamarock, and B. Eder (2005), Fully coupled online chemistry within the WRF_Chem model, *Atmos. Environ.*, *39*, 6957–6975.

Gyawali, M., W. P. Arnott, K. Lewis, and H. Moosmuller (2009), In situ aerosol optics in Reno, NV, USA during and after the summer 2008 California wildfires and the influence of absorbing and non-absorbing organic coatings on spectral light absorption, *Atmos. Chem. Phys.*, *9*, 8007–8015.

Hadley, O. L., V. Ramanathan, G. R. Carmichael, Y. Tang, C. E. Corrigan, G. C. Roberts, and G. S. Mauger (2007), Trans- Pacific transport of black carbon and fine aerosols (D < 2.5 mm) into North America, *J. Geophys. Res.*, *112*, D05309, doi:10.1029/2006JD007632.

Hadley, O. L., C. E. Corrigan, T. W. Kirchstetter, S. S. Cliff, and V. Ramanathan (2010), Measured black carbon deposition on the Sierra Nevada snow pack and implication for snow pack retreat, *Atmos. Chem. Phys.*, *10*, 7505–7513, doi:10.5194/acp-10-7505-2010.

Hess, M., P. Koepke, and I. Schult (1998), Optical properties of aerosols and clouds: The software package OPAC, *Bull. Am. Meteorol. Soc.*, *79*, 831–844.

Holben, B. N., et al. (2001), An emerging ground-based aerosol climatology: Aerosol optical depth from AERONET, *J. Geophys. Res.*, *106*(11), 12,067–12,097, doi:10.1029/2001JD900014.

Hsu, N. C., R. Gautam, A. M. Sayer, C. Bettenhausen, C. Li, M. J. Jeong, S.-C. Tsay, and B. N. Holben (2012), Global and regional trends of aerosol optical depth over land and ocean using SeaWiFS measurements from 1997 to 2010, *Atmos. Chem. Phys.*, *12*(17), 8037–8053, doi:10.5194/acp-12-8037-2012.

Jacobson, M. Z. (1999), Isolating nitrated and aromatic aerosols and nitrated aromatic gases as sources of ultraviolet light absorption, *J. Geophys. Res.*, *104*(D3), 3527–3542.

Jacobson, M. Z. (2010), Short-term effects of controlling fossil-fuel soot, biofuel soot and gases, and methane on climate, Arctic ice, and air pollution health, *J. Geophys. Res.*, *115*, D14209, doi:10.1029/2009JD013795.

Kahn, R. A., D. Nelson, M. Garay, R. Levy, M. Bull, D. Diner, J. Martonchik, S. Paradise, E. Hansen, and L. Remer (2009), MISR Aerosol Product Attributes and Statistical Comparisons With MODIS, *IEEE Trans. Geosci. Remote Sens.*, *47*(12), 4095–4114, doi:10.1109/TGRS.2009.2023115.

Kahn, R. A, B. J. Gaitley, M. J. Garay, D. J. Diner, T. F. Eck, A. Smirnov, and B. N. Holben (2010), Multiangle Imaging SpectroRadiometer global aerosol product assessment by comparison with the Aerosol Robotic Network, *J. Geophys. Res.*, *115*, D23209, doi:10.1029/2010JD014601.

Kanakidou, M., et al. (2005), Organic aerosol and global climate modeling a review, *Atmos. Chem. Phys.*, *5*, 1053–1123, doi:10.5194/acp-5-1053-2005.

Kato, S., T. P. Ackerman, J. H. Mather, and E. E. Clothiaux (1999), The k-distribution method and correlated-k approximation for a shortwave radiative transfer model, *J. Quant. Spectros. Radiat. Transfer*, *62*, 109–121, doi:10.1016/S0022-4073(98)00075-2.

Kim, D., and V. Ramanathan (2008), Solar radiation budget and radiative forcing due to aerosols and clouds, *J. Geophys. Res.*, *113*, D02203, doi:10.1029/2007JD008434.

Kim, D., and V. Ramanathan (2012), Improved estimates and understanding of global albedo and atmospheric solar absorption, *Geophys. Res. Lett.*, *39*, L24704, doi:10.1029/2012GL053757.

Kirchstetter, T. W., T. Novakov, and P. V. Hobbs (2004), Evidence that the spectral dependence of light absorption by aerosols is affected by organic carbon, *J. Geophys. Res.*, *109*, D21208, doi:10.1029/2004JD004999.

Kirchstetter, T. W., J. Aguiar, S. Tonse, T. Novakov, and D. Fairley (2008), Black carbon concentrations and diesel vehicle emission factors derived from coefficient of haze measurements in California: 1967-2003, *Atmos. Environ.*, *42*(3), 480–491.

Koch, D., T. C. Bond, D. Streets, N. Unger, and G. R. van der Werf (2007), Global impacts of aerosols from particular source regions and sectors, *J. Geophys. Res.*, *112*, D02205, doi:10.1029/2005JD007024.

Koch, D., and A. D. Del Genio (2010), Black carbon semi-direct effects on cloud cover: Review and synthesis, *Atmos. Chem. Phys.*, *10*, 7685–7696.

Lau, K. M., and K. M. Kim (2006), Observational relationships between aerosol and Asian monsoon rainfall, and circulation, *Geophys. Res. Lett.*, *33*, L21810, doi:10.1029/2006GL027546.

Lack, D. A., and C. D. Cappa (2010), Impact of brown and clear carbon on light absorption enhancement, single scatter albedo and absorption wavelength dependence of black carbon, *Atmos. Chem. Phys.*, *10*, 4207–4220, doi:10.5194/acp-10-4207-2010.

Lynn, B., A. Khain, D. Rosenfeld, and W. L. Woodley (2007), Effects of aerosols on precipitation from orographic clouds, *J. Geophys. Res.*, *112*, D10225, doi:10.1029/2006JD007537.

Magi, B. I., P. Ginoux, Y. Ming, and V. Ramaswamy (2009), Evaluation of tropical and extratropical Southern Hemisphere African aerosol properties simulated by a climate model, *J. Geophys. Res.*, *114*, D14204, doi:10.1029/2008JD011128.

Mao, Y. H., Q. B. Li, L. Zhang, Y. Chen, J. T. Randerson, D. Chen, and K.-N. Liou (2011), Wildfire contribution to black carbon in the western U.S. mountain ranges, *Atmos. Chem. Phys.*, *11*, 11,253–11,266, doi:10.5194/acp-11-11253-2011.

Menon, S., J. Hansen, L. Nazarenko, and Y. Luo (2002), Climate effects of black carbon aerosols in China and India, *Science*, *297*, 2250–2253.

Moosmuller, H., R. K. Chakrabarty, K. M. Ehlers, and W. P. Arnott (2011), Absorption Ångström coefficient, brown carbon, and aerosols: Basic concepts, bulk matter, and spherical particles, *Atmos. Chem. Phys.*, *11*, 1217–1225.

Myhre, G., C. R. Hoyle, T. F. Berglen, B. T. Johnson, and J. M. Haywood (2008), Modeling of the solar radiative impact of biomass burning aerosols during the Dust and Biomass-burning Experiment (DABEX), *J. Geophys. Res.*, *113*, D00C16, doi:10.1029/2008JD009857.

Nenes, A., W. C. Conant, and J. H. Seinfeld (2002), Black carbon radiative heating effects on cloud microphysics and implications for the aerosol indirect effect, 2. Cloud microphysics, *J. Geophys. Res.*, *107*(D21), 4605, doi:10.1029/2002JD002101.

Pincus, R., H. W. Barker, and J.-J. Morcrette (2003), A fast, flexible, approximate technique for computing radiative transfer in inhomogeneous cloud fields, *J. Geophys. Res.*, *108*(D13), 4376, doi:10.1029/2002JD003322.

Podgorny, I. A., and V. Ramanathan (2001), A modeling study of the direct effect of aerosols over the tropical Indian Ocean, *J. Geophys. Res.*, *106*(D20), 24,097–24,105, doi:10.1029/2001JD900214.

Ramanathan, V., P. J. Crutzen, J. T. Kiehl, and D. Rosenfeld (2001), Aerosols, climate, and the hydrological cycle, *Science*, *294*, 2119–2124.

Roden, C. A., T. C. Bond, S. Conway, A. Benjamin, and O. Pinel (2006), Emission factors and real-time optical properties of particles emitted from traditional wood burning cookstoves, *Environ. Sci. Technol.*, *40*, 6750–6757.

Rossow, W. B., and R. A. Schiffer (1999), Advances in understanding clouds from ISCCP, *Bull. Am. Meteorol. Soc.*, *80*, 2261–2287.

Russell, P. B., R. W. Bergstrom, Y. Shinozuka, A. D. Clarke, P. F. Decarlo, J. L. Jimenez, J. M. Livingston, J. Redemann, O. Dubovik, and A. Strawa (2010), Absorption Angstrom Exponent in AERONET and related data as an indicator of aerosol composition, *Atmos. Chem. Phys.*, *10*(3), 1155–1169.

Torres, O., A. Tanskanen, B. Veihelmann, C. Ahn, R. Braak, P. K. Bhartia, P. Veefkind, and P. Levelt (2007), Aerosols and surface UV products from Ozone Monitoring Instrument observations: An overview, *J. Geophys. Res.*, *112*, D24S47, doi:10.1029/2007JD008809.

Veefkind, J. P., J. F. de Haan, E. J. Brinksma, M. Kroon, and P. F. Levelt (2006), Total ozone from the Ozone Monitoring Instrument (OMI) using the DOAS technique, *IEEE Trans. Geosci. Remote Sens.*, *44*(5), 1239–1244.

Westerling, A. L., H. G. Hidalgo, D. R. Cayan, and T. W. Swetnam (2006), Warming and earlier spring increase western US forest wildfire activity, *Science*, *313*(5789), 940–943.

Wielicki, B. A., B. R. Barkstrom, E. F. Harrison, R. B. Lee, G. L. Smith, and J. E. Cooper (1996), Clouds and the Earth's Radiant Energy System (CERES): An Earth observing system experiment, *Bull. Am. Meteorol. Soc.*, *77*, 853–868.

Wilcox, E. M. (2010), Stratocumulus cloud thickening beneath layers of absorbing smoke aerosol, *Atmos. Chem. Phys.*, *10*, 11,769–11,777, doi:10.5194/acp-10-11769-2010.

Yang, M., S. G. Howell, J. Zhuang, and B. J. Huebert (2009), Attribution of aerosol light absorption to black carbon, brown carbon, and dust in China – interpretations of atmospheric measurements during EAST-AIRE, *Atmos. Chem. Phys.*, *9*, 2035–2050.

Young, S. A., and M. A. Vaughan (2009), The retrieval of profiles of particulate extinction from Cloud Aerosol Lidar Infrared Pathfinder Satellite Observations (CALIPSO) data: Algorithm description, *J. Atmos. Oceanic Technol.*, *26*, 1105–1119.

Zhao, C., L. R. Leung, R. Easter, J. Hand, and J. Avise (2013), Characterization of speciated aerosol direct radiative forcing over California, *J. Geophys. Res. Atmos.*, *118*, 2372–2388, doi:10.1029/2012JD018364.